Discovery of Novel Allosteric Sites of SARS-CoV-2 Papain-Like Protease (PLpro)

Juliana C. Ferreira[1], Kenana Al Adem[1], Samar Fadl[1], Adrian J. Villanueva[1], Lara Alzyoud[2,3], Mohammad A Ghattas[2,3] and Wael M. Rabeh[1, *]

1 Science Division, New York University Abu Dhabi, PO Box 129188, Abu Dhabi, United Arab Emirates.

2 College of Pharmacy, Al Ain University, Abu Dhabi 64141, United Arab Emirates

3 AAU Health and Biomedical Research Center, Al Ain University, Abu Dhabi 64141, United Arab Emirates

*Corresponding author: wael.rabeh@nyu.edu

Keywords: COVID-19, SARS-CoV-2, papain-like protease (PLpro), allosteric sites, thermodynamic stability, initial velocity studies.

Abstract

Papain-like protease (PLpro) is a viral protease found in some coronaviruses, including SARS-CoV-2, the virus that causes COVID -19, and is a target for antiviral drug development. Inhibition of PLpro activity could potentially limit viral replication, making it an attractive target for antiviral drug development. This work describes the discovery of novel allosteric residues of SARS-CoV-2 PLpro that can be targeted with antiviral drugs. First, a computational analysis was performed to identify potential druggable pockets on the surface of SARS-CoV-2 PLpro. The computational analysis predicted three druggable pockets that span the surface of PLpro and are located at the interface of its four domains. Pocket 1 is located at the interface between the Ub1 and thumb domains, pocket 2 is at the interface between the thumb, finger, and palm domains, and pocket 3 is at the interface between the finger and palm domains. Targeted alanine mutagenesis of selected residues with important structural interactions revealed that 12 of 23 allosteric residues (D12, Y71, Y83, Q122, Q133, R140, T277, S278, S212, Y213, K254, and Y305) are essential for maintaining a catalytically active and thermodynamically stable PLpro. This work provides experimental confirmation of essential contacts in the allosteric sites of PLpro that could be targeted with non-competitive inhibitors as novel therapeutics against COVID -19.

Introduction

As the globe anticipates the subsidence of the reported number of new coronavirus disease 2019 (COVID-19) cases, scientists continue on racing to develop more antivirals against severe acute respiratory syndrome-coronavirus 2 (SARS-CoV-2) to combat the impending threat of viral mutations and antiviral resistance. In the past three years, the world has witnessed sequential outbreaks of SARS-CoV-2 variants that resulted in waves of worldwide infection with symptoms that ranged between influenza-like symptoms and acute lower respiratory infections accompanied by dyspnea and pneumonia (Lan, Filler et al. 2020). Since its emergence in December 2019 in Wuhan, China, the World Health Organization (WHO) has reported more than 700 million cases and over 6 million deaths (Shetler, Ferreira et al. 2022, WHO 2022). SARS-CoV-2 is a single-stranded RNA virus having characteristic crown-like projections displayed on its surface (Wu, Wu et al. 2020, Chadha, Khullar et al. 2022), with the viral ability to encode for four different structural proteins, namely, Spike (S), Envelope (E), Membrane (M), and Nucleocapsid (N) proteins (Kaur and Gupta 2020).

The entry of SARS-CoV-2 into the host cell is initiated by the S protein when it binds to angiotensine-converting enzyme 2 (ACE2), the main host cell receptor, via the S1 subunit of the spike protein (Zhang, Xiang et al. 2021, Jackson, Farzan et al. 2022). Subsequently, SARS-CoV-2 begins entry into the cell through a membrane-fusion step via the S2 subunit of the spike protein (Li 2016). Upon entry into the cell, the viral genomic RNA is introduced into the host cell and is then translated into non-structural (nsps) polyproteins by means of two open reading frames (ORFs), ORF1a and ORF1b, that produce two polyproteins, pp1a and pp1ab, respectively (Kim, Lee et al. 2020, V'Kovski, Kratzel et al. 2021). PLpro is required for the proteolytic release of nsp 1-4, whereas 3CLpro is required for the proteolytic release of nsp 5 – 16 (Krichel, Falke et al. 2020, Wu, Chen et al. 2020).

Not only do nsps play a critical role in viral transcription and replication, but they also counteract the host innate immunity responses. Thus, the study of nsp assemblies and functions provides a foundation for the development of novel drugs targeting viral infections and immune evasion machinery (Rohaim, El Naggar et al. 2021, Shetler, Ferreira et al. 2022). Previous studies have shown that PLpro from various coronaviruses has an antagonistic ability to evade the innate immune system of the host and start viral replication. The mechanism involves the inhibition of the phosphorylation and nuclear translocation of the interferon regulatory factor-3 (IRF3) by PLpro polyprotein, resulting in deactivation of the

type I interferon (IFN) response (Chen, Yang et al. 2014). Moreover, the processes of ISGylation and ubiquitination are key elements in the activation of the innate immune response, which, if disrupted by a virus, would lead to successful viral infection. In fact, PLpro was reported to have deubiquitination properties (DUB) homologous to human deubiquitinases. This allows PLpro to cleave ubiquitin and ubiquitin-like modifiers such as interferon-stimulated gene 15 (ISG15), which is known to be induced during viral infections. Consequently, inflammation and antiviral signalling of the immune system are inhibited by PLpro domain. As a result, the host's ability to recognize and degrade the invading viral proteins is hindered (Yang, Chen et al. 2014, Klemm, Ebert et al. 2020). Thus, considering the structural and functional properties of PLpro would allow the development of antiviral drugs against various coronaviruses such as SARS-CoV-2, SARS-CoV, and MERS-CoV.

The tertiary structure of SARS-CoV-2 PLpro monomer adopts a right-handed conformation composed of two main domains, namely the ubiquitin-like (Ub1) domain and the catalytic domain (Ferreira, Pillaiyar et al. 2022). The N-terminal Ub1 domain of PLpro consists of residues 1 – 60, which form 5 β-strands, a single α-helix and a single 3_{10} helix. The catalytic domain is further divided into three main subdomains responsible for enzyme activity: Thumb, Finger, and Palm domains (Ferreira, Pillaiyar et al. 2022). The thumb domain (61 - 176) has 6 α-helices and two small β-strands, while the finger domain (177 - 238) contains the zinc binding site and consists of 5 β-strands and two α-helices. The palm domain spans residues 239 - 315 and consists of 6 β-strands. The catalytic site of PLpro is located between the thumb and palm subdomains and consists of three amino acids (Cys111, His272, and Asp286), known as the "catalytic triad", that are essential for the proteolytic mechanism of the enzyme (Baez-Santos, St John et al. 2015, Klemm, Ebert et al. 2020, Osipiuk, Azizi et al. 2021). The Ub1 domain binds ubiquitin or ISG15 in an "open hand" structure, with ubiquitin resting on the palm subdomain. The zinc-binding finger, consisting of four conserved cysteine residues (C189, C192, C224, and C226), holds the ubiquitin in place and is an essential component for the structural integrity and activity of the protease (Lv, Cano et al. 2021). Previous studies have shown that alanine substitution of the cysteine residues in the zinc-binding domain would result in complete loss of PLpro function (Barretto, Jukneliene et al. 2005).

Due to the highly rapid and destructive proliferation of SARS-CoV-2 across the globe, the scientific community has witnessed the development of therapeutic drugs for COVID-19

treatment at an unprecedented rate. In the early stages of the COVID-19 pandemic, many research efforts have turned to drug-repurposing, a strategy that involves testing a collection of approved or investigational drugs against SARS-CoV-2 targets, like 3CLpro and PLpro (Pushpakom, Iorio et al. 2019, Cavasotto and Di Filippo 2021, Kandeel, Abdelrahman et al. 2021, Luo, Qiu et al. 2021). Owing to the immediate meteoric rise in the prevalence of COVID-19 in early 2020 and the urgency created along with it, a drug-repurposing strategy was viewed as a promising course of action, in hopes of accelerating the development of COVID-19 treatments. Numerous *in-silico* attempts have been made in repurposing drugs to target SARS-CoV-2 PLpro, but putative drug candidates still remain to be biochemically confirmed (Klemm, Ebert et al. 2020, Smith, Davis-Gardner et al. 2020, Redhead, Owen et al. 2021, Xu, Chen et al. 2021, Zhao, Du et al. 2021). Meanwhile, several repurposed drug candidates against PLpro have gained traction when tested in-vivo or in-vitro – Simeprivir, Tanshinone, Famotidine and Ebselen, to name a few (Jin, Du et al. 2020, Gammeltoft, Zhou et al. 2021, Lim, Tan et al. 2021, Mura, Preissner et al. 2021), https://doi.org/10.21203/rs.3.rs-26344/v1. However, these drug candidates are either found clinically ineffective, are still under clinical trials, or still require thorough biochemical assessment (Calleja, Lessene et al. 2022). Screening for novel small-molecule inhibitors against PLpro is an alternative, but costly and time-consuming, strategy (Amin, Ghosh et al. 2021, Quimque, Notarte et al. 2021, Gogoi, Borkotoky et al. 2022, Jiang, Yang et al. 2022). Upon identification of a drug lead, potential inhibitors are often subjected to further optimization and drug design to improve potency and selectivity (Shan, Liu et al. 2021, Weglarz-Tomczak, Tomczak et al. 2021). By screening a vast collection of molecules and carrying out further drug optimizations on lead molecules, inhibitors can reach a potency down to the nanomolar order of magnitude (Ma, Sacco et al. 2021, Shan, Liu et al. 2021). Lastly, zinc-ejecting drugs have also been shown to have inhibitory potential against PLpro. They are a class of inhibitors which aim at targeting the metalloenzymes that have a common zinc-finger motif, like that in PLpro. Several zinc-ejecting drugs have been approved by the Food and Drug Administration (FDA) and are currently on the market. The mechanism behind these drugs is to disrupt the zinc-cysteine tetrahedral complex by means of displacing the metal ion (Shetler, Ferreira et al. 2022). However, there is an emerging debate regarding the efficacy of zinc-ejecting drugs; molecular dynamics studies on PLpro suggest that the labile zinc finger subdomain is a highly mobile region, making the zinc-finger structural motif a poor drug target as it would prove challenging for small molecule drugs to bind to tightly (Bosken, Cholko et al. 2020). On the other hand, some studies have reported that zinc-

ejecting drugs, such as ebselen and disulfiram, disrupt the stability of PLpro, thereby reducing its catalytic activity. These findings suggest the possibility of using zinc-ejecting drugs together with other antiviral drugs to treat COVID-19 symptoms in a so-called "multi-target approach" (Lin, Moses et al. 2018, Ma, Hu et al. 2020, Sargsyan, Lin et al. 2020, Calleja, Lessene et al. 2022).

Nonetheless, the world is still pressed for the development of an effective therapeutic agent against COVID-19. Out of the potential targets against SARS-CoV-2, PLpro remains to be an exceptional protein of interest as it plays a dual role in viral replication and evasion of the antiviral immune response. Herein, we identified three novel binding pockets in SARS-CoV-2 PLpro *in-silico*. Inside each of the identified binding pockets, selected amino acid residues with important structural interactions were biochemically and thermodynamically characterized *in-vitro* after site-directed mutagenesis. Mutagenesis studies were conducted to confirm the druggability of these identified binding pockets from our computational findings. This research study is aimed to aid the development of novel non-competitive drugs that can allosterically bind and inhibit PLpro and ultimately be used as a therapeutic drug in our efforts to combat the spread of COVID-19.

Materials and Methods

Selection and preparation of PLpro crystal structures

The Protein Data Bank was used to download all PLpro crystal structures used in this work (http://www.rcsb.org). All structures considered were solved using X-crystallography and contained no mutated residues; otherwise, they were discarded. Overall, 22 PLpro crystal structures were included in the analysis.

Each structure was then prepared by MOE [1]. The solvent atoms from each crystal structure were removed, and any missing atoms, residues, chains, or loops were added using the protein preparation module. Then, Protonate3D was used to assign each atom a unique protonation state. The prepared crystal structures were then imported into Maestro [2], where the Protein Preparation wizard [3] module is used to refine proteins to maintain structural integrity. Hydrogens were added using hydrogen bond optimization, and the structures were then subjected to restrained minimization to achieve a reduced energy state.

Druggability Assessment of allosteric sites

The SiteMap[4] module was used to process proteins, with all settings left at their default. To prevent any bias from utilizing ligands or peptides to identify pockets, the "Identify top-ranked possible receptor binding sites" option was used. SiteMap computes numerous physiochemical parameters for each site, such as size, exposure, hydrophobicity, hydrophilicity, and volume [5]. Most significantly, it assigns a Dscore to each protein binding pocket using a weighted equation:

$$\text{Dscore} = 0.094\sqrt{n}+0.60e-0.324p \qquad \text{(equation 1)}$$

Where n denotes the number of site points, e denotes the enclosure factor, and p denotes the hydrophilicity.

Analyzing scores obtained by SiteMap

To analyze the Dscores produced by SiteMap [4], Halgren [5] proposed a classification system with a threshold to differentiate druggable sites from difficult sites. This approach can correctly predict the ligand binding site in 86% of protein-ligand complexes according to their Dscores. Sites are classified as difficult if their Dscore is less than 0.8, druggable if their Dscore is between 0.8 and 1.0, and very druggable if their Dscore is greater than 1.0.

Expression and purification of WT and PLpro mutants

The recombinant PLpro wild type and mutants' genes with an N-terminal Hisx6 tag was introduced into the pET-28b (+) bacterial expression vector by GenScript, Inc. (Piscataway, NJ). The vector was used to transform E. coli BL21-CodonPlus-RIL (Stratagene) for protein expression as described previously (Shetler, Ferreira et al. 2022). The inoculated culture (5 L) was grown at 30 °C in lysogeny broth (LB) with 100 mg/L kanamycin, 50 mg/L chloramphenicol, and 1 μM ZnCl2 until the absorbance at 600 nm reached 0.5. The temperature was then reduced to 15 °C, and protein expression was induced overnight (14-16 h) by adding 1 mM IPTG. The cells were pelleted by centrifugation at 12,000 xg and 4 °C for 10 min in an Avanti J26-XPI centrifuge (Beckman Coulter Inc.). The cell pellets were homogenized in lysis buffer (25 mM Tris, 150 mM NaCl, 5 mM imidazole, 3 mM β-mercaptoethanol (βME), and 0.1% protein inhibitor cocktail (Sigma-Aldrich: P8849) before sonication on ice. The cell lysate was then centrifuged at 40,000 xg and 4 °C for 45 min. The supernatant was loaded onto a nickel column pre-equilibrated with binding buffer (25 mM Tris, 150 mM NaCl, 5 mM imidazole, and 3 mM βME). The column was washed with binding buffer supplemented with 25 mM imidazole, followed by elution with binding buffer

supplemented with 300 mM imidazole. The nickel column fractions containing PLpro were pooled and loaded onto a HiLoad Superdex 200 size-exclusion column (GE Healthcare) on an ÄKTA pure 25 chromatography system (Cytiva, USA). The gel filtration column was pre-equilibrated with 20 mM HEPES pH 7.5, 150 mM NaCl, and 0.5 mM tris(2-carboxyethyl)phosphine (TCEP). The PLpro-containing fractions were collected and concentrated to ~150 μM. The sample concentration and purity were determined by the Bradford assay and SDS-PAGE, respectively.

Enzyme titration and initial velocity studies

PLpro enzyme titration and initial velocity analyses were performed using a Cytation 5 multi-mode microplate reader (BIOTEK Instruments, Winooski, VT), as described previously (Shetler, Ferreira et al. 2022). The peptide substrate contained the PLpro cleavage site Leu-Arg-Gly-Gly flanked by a fluorescent AMC (7-amino-4-methyl coumarin) tag and corresponding quencher CBZ (carbobenzoxy) (*i.e.*, Z-LRGG-AMC). The proteolytic reaction was initiated by adding 0.5 μM PLpro enzyme to the peptide in buffer (50 mM HEPES pH 7.5, 0.5 mM EDTA, and 0.5 mM TCEP) containing 2% DMSO to enhance the solubility of the peptide (Ferreira, Fadl et al. 2021). The PLpro reaction was monitored in a 96-well microplate at 25 °C for 10 min at excitation and emission wavelengths of 340 nm and 487 nm, respectively. Cleavage of the peptide substrate by PLpro resulted in an increase in the AMC fluorescent signal.

To assess the effect of a single amino acid substitution on the rate of proteolysis by PLpro, the enzymatic activity of the WT enzyme and mutants was first assayed at different enzyme concentrations. The concentration of the peptide substrate was fixed at 200 μM, and the enzyme concentration was varied from 0.5 to 5 μM. Next, initial velocity studies were performed with the WT enzyme and the catalytically active mutants to determine K_m and k_{cat}. The concentration of the peptide substrate was varied from 20 to 500 μM at a fixed concentration of PLpro. The cleavage rate data were fit to the Michaelis–Menten equation using the global fitting analysis function in the kinetics module of SigmaPlot (Systat Software, Inc). Error bars were calculated from triplicate measurements of each reaction, and the results are presented as the mean ± SD.

Thermal Inactivation of PLpro WT and mutants

The thermal inactivation of PLpro variants was carried out by measuring the rates of enzyme sample incubated at 37 °C at different time intervals. The enzymatic activity of PLpro was

determined as described above. Using Prism 9 (GraphPad Software), the decay in enzymatic activity was fitted to a one phase decay equation:

$$A = A_0 e^{-kt} \ (Eq.\ 2)$$

Where A is the relative activity of the enzyme at incubation time t, A_0 is the activity of the enzyme at t=0, and k is the rate constant. The half-life ($t_{1/2}$) was defined to be the time at which enzymatic activity was reduced to half, which is equal to $\frac{ln\ (2)}{k}$.

Results

Structural assessment of putative binding sites on SARS-CoV-2 PLpro

PLpro is composed of 4 main domains including Ub1, thumb, finger and palm domains. The secondary structural arrangements of the four PLpro domains result in a right-handed conformation of the monomeric unit of PLpro. Here, we used SiteMap module to identify potential druggable pockets on the surface of SARS-CoV-2 PLpro. SiteMap analysis revealed 5 top-ranked potential binding sites on PLpro that were assigned druggability scores based on their physiochemical parameters. Of the predicted pockets, the active site of PLpro and another small allosteric site located on the same side of the active site were assigned the highest druggability scores (**Figure S1**). On the other hand, three additional allosteric pockets, located at the opposite side of the active site have been identified with moderate druggability scores presumably due to their shallow nature (**Figure S1**). **Table 1** illustrates the distinctive physiochemical parameters of the predicted binding sites on PLpro surface. The small allosteric site, which received the highest ranking, has a large (n = 62 spheres), well-defined pocket (e = 0.67), with moderate hydrophilicity (p = 0.53). The other druggable pocket is the PLpro active site that has also shown a large (n = 75 spheres), slightly more defined (e = 0.68) cavity but with significantly higher hydrophilicity (p = 0.99). In addition, three other putative allosteric pockets have been identified on PLpro surface with variable cavity sizes (**Table 1**). Pocket 1 resembles the small allosteric site in terms of its size (n = 61 spheres) and enclosure (e = 0.67), but due to its very high hydrophilicity (p = 1.02) its Dscore measures 0.74. Pockets 2 and 3, have smaller (n = 29 and 31 spheres, respectively), less defined cavities (e = 0.58 and 0.62) and higher hydrophilicity (p = 0.89 and 0.99) with lower druggability scores (Dscore = 0.56 and 0.57), respectively.

The main objective of this study is to identify potential druggable pockets on SARS-CoV-2 PLpro surface that can allosterically regulate the enzyme activity. These allosteric pockets can be used as potential targets for the development of new drugs to combat COVID-19. The computational analysis described above predicted three potential allosteric pockets located at the opposite side of PLpro active site. The three predicted pockets span different regions of PLpro and are located at the interface of its four domains including Ub1-thumb, thumb-palm and finger-palm domains as will be detailed below. The residues forming these three pockets are shown in **Table S1** and **Figure S1**.

Next, we identified key residues in each of pockets 1 – 3 that were proposed to be important for PLpro activity due to their polar side chain interactions with other residues (**Figures 1 – 3**). Residues with side-chain interactions may have critical roles in maintaining the structural stability and catalytic activity of SARS-CoV-2 PLpro. Using site-directed mutagenesis, the selected residues will be experimentally characterized to determine their effect on PLpro enzymatic activity and thermodynamic stability.

Table 1. Mean values of druggability score (Dscore) and other SiteMap physiochemical parameters obtained from the 22 PLpro structures studied in this work.

Site	Dscore	Size	Enclosure	Hydrophilicity
Allosteric Site	0.97	62	0.67	0.53
Active Site	0.88	75	0.68	0.99
Pocket 1	0.74	61	0.67	1.20
Pocket 2	0.56	29	0.58	0.89
Pocket 3	0.57	31	0.62	0.99

<u>Pocket 1: Interface between Ub1 and thumb domains</u>

Pocket 1 is located away from the active site at the interface between the Ub1 and thumb domains (**Figure S1**). In pocket 1 at Ub1 domain, the side chain of T10 forms an intra-domain hydrogen bond with the main chain nitrogen of D12 at 3.3 Å (**Figure 1A**). In addition, Y71 from the thumb domain can form two possible hydrogen bonding interactions, an inter-domain one with the main chain of D12 at 4.2 Å and an intra-domain one with the side chain of D134 at 2.7 Å. Next, an inter-domain hydrogen bonding interaction is predicted

between the hydroxyl side chain of Y72 (thumb domain) and the backbone carbonyl oxygen of V11 (Ub1 domain) at a distance of 2.6 Å.

The side chain of D12 is predicted to have 3 polar intra-domain interactions with the backbone nitrogen of I14 at 2.8 Å, and the side chain and backbone atoms of N15 at 2.7 and 2.8 Å, respectively (**Figure 1B**). In addition, the side chain carbonyl oxygen of N15 (Ub1 domain) is predicted to form an inter-domain polar interaction with the side chain of E67 (thumb domain) at 4.4 Å. In turn, E67 side chain is expected to have another inter-domain polar interaction with the imidazole group of H17 (Ub1 domain) at 3.4 Å (**Figure 1B**).

In pocket 1, several intra-domain interactions are detected within Ub1 and thumb domains (**Figure 1C**). The intra-domain interactions within Ub1 are seen between the side chain nitrogen and carbonyl oxygen of N13 that form hydrogen bonds with T54 and Y56 and at 4.7 and 4.2 Å, respectively (**Figure 1C**). In turn, the side chain of Y56 is predicted to have a polar inter-domain interaction with the side chain of Y83 (thumb domain) at 4.5 Å. In pocket 1, the thumb domain is predicted to have several intra-domain interactions initiated by the residues Y83, R138, E143 and N146 (**Figure 1C**). First, a polar interaction is observed between the side chains of Y83 and N146 at 2.6 Å. Also, the side chain carbonyl oxygen of N146 forms a polar interaction (3.4 Å) with R138 side chain. In turn, R138 side chain is predicted to have a salt-bridge interaction (3.1 Å) with E134 side chain.

Lastly, an inter-domain interaction is detected between the side chain of K91 (thumb domain) and the backbone of D37 (Ub1 domain) at 2.8 Å. Additionally, K91 side chain is predicted to have another possible polar interaction with the side chain of N88 side chain at 2.9 Å (**Figure 1D**).

<u>Pocket 2: Interface between thumb, finger, and palm domains</u>

Pocket 2 is mainly located between the thumb and palm domains and only a few residues are from the finger domain (**Figure S1**). First, at the interface of thumb and palm domains, T115, T119 and Q122, all from thumb domain, form several inter-domain interactions with H275 and T277, both from the palm domain (**Figure 2A**). The side chain of Q122 initiates two polar interactions with the imidazole group of H275 at 2.8 Å and with the hydroxyl side chain of T277 at 2.7 Å. The side chain of T277 may also be involved in a long intra-domain polar interaction (5.1 Å) with K279 side chain. The imidazole group of H275 is also detected to

form two polar inter-domain interactions with the side chains of T115 and T119 at 3.0 and 3.6 Å, respectively.

In pocket 2, the second inter-domain site is found at the interface between the thumb and finger domains where N128 side chain (thumb domain) forms a hydrogen bond with the backbone nitrogen of N177 (finger domain) at 3.9 Å. In turn, N177 side chain forms an intra-domain hydrogen bond with D179 side chain at 3.7 Å. Within the finger domain, Q133 side chain forms two polar intra-domain interactions with the side chains of K126 and N128 at 3.5 and 3.3 Å, respectively.

The third inter-domain site in pocket 2 is found at the interface between the finger and palm domains where the side chains of Q236 and E238 (finger domain) form polar interactions with the side chains of T311 and S309 (palm domain), respectively (**Figure 2C**). In addition, the Q236 and E238 form another intra-domain interaction between their side chains at a distance of 2.4 Å. At the same site, the side chains of Q237 and S239 form an inter-domain hydrogen bond at 3.0 Å (**Figure 2C)**. In pocket 2, several intra-domain interactions occur in the palm (**Figure 2A**) and thumb (**Figure 2D**) domains. In the palm domain, the side chain of S278 forms three possible polar interactions with the backbone atoms of G256 and K279 at 2.9 and 3.7 Å, respectively and with the imidazole of H255 at 4.2 Å. Also, the imidazole of H255 in the palm domain is expected to form a hydrogen bond with the backbone carbonyl oxygen of K279 at 2.7 Å (**Figure 2D**). The intra-domain interactions within the thumb domain in pocket 2 are formed between the side chain of R140 with the side chain of Y136 and the main chain of Q121 at 2.8 and 3.2 Å, respectively (**Figure 2D**).

<u>Pocket 3: Interface between finger and palm domains</u>

Pocket 3 is located at the interface between the finger and palm domains. Several residues in pocket 3 have inter-domain side chain interactions. First, the side chain hydroxyl group of Y213 (finger domain) interacts with the side chain of E307 (palm domain) at 2.5 Å (**Figure 3A**). Also, Y213 main chain has intra- and inter-domain interactions with S212 side chain and Y305 at distances of 3.4 Å and 3.5 Å, respectively. In turn, the hydroxyl side chain of Y305 is predicted to have another possible intra-domain hydrogen bond with side chain of Y251 (4.1 Å). In pocket 3, the side chain of K306 in the palm domain has intra- and inter-domain hydrogen bonds with T259 side chain and main chain of Q122 (thumb domain) at 4.3 Å and 4.2 Å, respectively (**Figure 3B)**. Also, some residues in pocket 3 were found to be

involved in intra-domain interactions only. The side chains of E214 and K217, both from the finger domain, form a salt-bridge interaction at 3.2 Å (**Figure 3A**). Also, E252, K254, T257 and E295, all from the palm domain, for intra-domain interactions (**Figure 3B)**. First, K254 side chain can form two possible polar interactions with the side chains of E252 and E295 at 3.6 and 34 Å, respectively. Lastly, the side chain hydroxyl group of T257 forms a hydrogen bond with the main chain carbonyl oxygen of K254 at 2.6 Å.

The structural analysis presented above provide detailed description of the possible intra-domain and inter-domain interactions between the residues within each computationally predicted allosteric pocket. The selected residues described here are proposed to have structural importance to the activity and stability of SARS-CoV-2 PLpro due to their localization at highly druggable pockets at PLpro surface. These residues will be first analyzed for their functional roles and structural stability on PLpro. Alanine substitution will be performed on these sites to eliminate their side chain interactions and determine their effects on the catalytic activity and thermodynamic stability of PLpro.

Relative enzyme activity of PLpro mutants at the three predicted allosteric pockets

Alanine site-directed mutagenesis was used to investigate the role of allosteric residues selected from the predicted druggable pockets of SARS-CoV-2 PLpro. A total of 23 alanine mutations were examined for their relative proteolytic activity compared with the wild-type PLpro enzyme. The proteolytic activity of PLpro WT and the mutants was measured in a reaction buffer with a pH of 7.5 and 20 mM HEPES, 100 mM NaCl, 1 mM TCEP, and 1 mM EDTA. Enzyme concentrations of PLpro WT or mutants were varied from 0.5 to 5 μM in the presence of a constant peptide substrate concentration of 200 μM. The relative enzymatic activity of each mutant was calculated by comparing the slope of the straight line for each mutant with that of WT.

<u>Pocket 1:</u>

Alanine mutations of D12, from Ub1 domain, and Y71, from the thumb domain, resulted in reduced catalytic rates with relative enzymatic activities of approximately 7.7% and 48%, respectively, compared with WT (**Figure 4A**). On the other hand, alanine substitution of D134, localized on α5 of the thumb domain, slightly enhanced PLpro activity with a rate of 102% (**Figure 4A**). This result indicates that the inter-domain polar interaction between the side chains of D12 and Y71 is vital for PLpro activity while the intra-domain interaction

between the side chains of Y71 and D134 does not affect the enzyme activity. Alanine mutation of Y83, localized at the α3 on the thumb domain, significantly decreased the enzyme activity with a rate of 11.5%. In contrast, R138A, E143A and N146A mutants, all in the thumb domain, increased the enzymatic rate of PLpro to 91%, 109% and 111%, respectively (**Figure 4B**). The allosteric residue, K91, localized at the α3 on thumb domain decreased PLpro activity by 35% (**Figure 4A**).

Pocket 2:

In pocket 2, alanine substitution of Q122, localized on the loop $^{121\text{-}129}$ between α4 and α5 on the thumb domain, decreased the activity by 65% (**Figure 4D and 4F**). The side chain of Q122 interacts with T277, localized in β9 on the palm domain, which in turn, decreased PLpro activity by 68% (Figure 3D and 3F). The side chain of T227 is also predicted to interact with K279, which is localized in loop$^{278\text{-}282}$ between β 9-10 on the palm domain, where K279A mutant slightly increased PLpro activity to 103% (**Figure 4D and 4F**). At the same site, S278, localized at loop $^{278\text{-}282}$ between β 9-10 on the palm domain, significantly reduced PLpro activity with a relative rate of 15.6% (**Figure 4D and 4F)**.

Alanine mutants of Q133, localized at α5 on the thumb domain, and N177, localized at loop $^{176\text{-}180}$ between α7 and β4 in the finger domain, decreased PLpro activity by 45% and 32%, respectively (**Figure 4D and 4F**). At the thumb domain in pocket 2, the side chain of Y136 interacts with the side chain of R140, and the alanine mutants of both residues decreased PLpro activity by 44% and 38%, respectively (**Figure 4E and 4F**). At the interface between the thumb and palm domains in pocket 2, E238, from the finger domain, decreased the enzymatic activity by 49% (**Figure 4E and 4F**).

Pocket 3:

In pocket 3, all the examined alanine mutants have either decreased or inactivated the activity of the enzyme. First, Y305 from the palm domain forms two possible inter-domain interactions with the side chains of S212 and Y213, both from the finger domain. Alanine mutants of Y213 and Y305 resulted in complete loss of the enzyme activity and S212A resulted in significant reduction of PLpro activity with a rate of 8.7% (**Figure 4H and 4I**). Alanine substitution of pocket 3 residues, E252 and K254, both forming intra-domain interactions within the palm domain, reduced the enzyme activity by 36% and 91%, respectively (**Figure 4G and 4I**). Lastly, K306, localized at the β13 of the palm domain, decreased PLpro activity by 47% (**Figure 4G and 4I**).

Initial velocity studies of PLpro mutants at the three predicted allosteric pockets

Initial velocity studies were performed to obtain the kinetic parameters, turnover number (k_{cat}), Michaelis constant (K_m) and the catalytic efficiency (k_{cat}/K_m), of PLpro mutants from the three predicted allosteric pockets (Figure 5). The initial velocity studies were only performed on enzymatically active PLpro mutants to examine their effects on the kinetic parameters of WT (Figure 4). PLpro inactive mutants could not be studied for their effects on kinetic parameters of the enzyme.

The alanine mutants: D12A, Y71A, and Y83A of the ubiquitin and thumb domains, pocket 1, decreased k_{cat} compared with the enzyme WT (Figure 4A). The reduction in k_{cat} ranged from 10-fold for D12A to 9-fold for Y83A to 2-fold for Y71A. Other mutants in pocket 1 did not show significant differences compared with WT. On the contrary, N146A had a high k_{cat} value compared with the WT enzyme (Figure 4A). Moreover, all mutants in pocket 1 exhibited similar affinity of the enzyme for the peptide substrate as WT, except for Y71A, which decreased K_m values by at least 2-fold compared with WT (Figure 4B). Accordingly, the catalytic efficiencies (k_{cat}/K_m) of all pocket-1 residues had similar values compared to WT enzyme (Figure 4C). In particular, D12A and Y83A had ~10-fold reduction in k_{cat}/K_m compared to WT enzyme, which is consistent with our previous results showing low relative enzyme rates of about 11% for D12A and Y83A (Figure 3C).

The pocket 2 alanine mutants, Q122A, T277A, and S278A, decreased k_{cat} by 3-fold, K_m by 1.4-fold, and k_{cat}/K_m by 60% compared with WT (Figure 4D - 4F). Mutants Q133A, N177A, Y136A, R140A, and E238A decreased k_{cat} by 1.6-fold, with similar K_m values to WT, except for residue E238A, which increased K_m by 1.5-fold and decreased k_{cat}/K_m by 50%, except for residues Q133A and Y136A, which were 10% and 20%, respectively (Figure 4D - F).

In pocket 3, alanine mutants reduced the k_{cat} of S212A, K254A, K306A and E252A, by 10-fold to S212A and K254A, by 1.8-fold and 1.3 fold to K306A and E252Am, respectively, as well as a 1.3-fold increase in K_m for S212A and E252A and decreased the k_{cat}/K_m values around 90% to S212A and K254A, and 30% to E252A and K306A (Figure 4G –I).

Thermal Inactivation of PLpro WT and mutants

Thermal inactivation studies were performed on PLpro WT and mutants to elucidate the relationship between stability and catalytic activity (**Figure 6**). PLpro variants were thermally inactivated by incubating enzyme samples in 37 °C and measuring the residual enzymatic

activity of enzyme variants at different time points. The incubation was carried out for two hours. PLpro variants that were found to be inactive in our titration experiments (**Figure 4**) were not included in this experiment. The half-life ($t_{1/2}$) was defined to be the time at which 50% relative activity was attained and was used as a quantitative measure of the kinetic stability of the PLpro variants. All half-life measurements of the PLpro mutants were analyzed in relation to the WT. Most PLpro mutants in pocket 1 were observed to have minimal effects on half-life (**Figure 6 A – C**). More notably, however, the half-life of K91A and Y71A mutants was found to be approximately twice that of the WT. Meanwhile, PLpro mutants in pocket 2 were found to be more kinetically unstable (**Figure 6 D – F**). N177A and E238A mutants decreased the half-life by 20% while T277A decreased half-life by 40%. Most importantly, Q122A and S278A mutants were found to have the fastest half-lives amongst all PLpro mutants tested here, decreasing its $t_{1/2}$ to almost 90%. Q133A and R140A mutants were observed to have a higher half-life than that of the WT by 24% and 15%, respectively. Lastly, PLpro mutants in pocket 3 have generally low half-lives, with the exception of K306A that had a 50% increase in $t_{1/2}$ (**Figure 6 G – I**). S212A, E252A, and K254A mutants recued $t_{1/2}$ of the WT PLpro by 30 – 50%.

Discussion

In the fight against COVID -19 and the spread of SARS-CoV-2, the discovery of antiviral drugs and the development of therapeutics are of great importance (Pushpakom, Iorio et al. 2019, Cavasotto and Di Filippo 2021, Kandeel, Abdelrahman et al. 2021, Luo, Qiu et al. 2021). A conserved step in the maturation of coronaviruses is the processing of the viral polyproteins to produce new virus particles. In addition to the main protease of SARS-CoV-2, the PLpro protease is responsible for the processing of the viral polyproteins and the release of functional proteins during viral infection, making it an attractive target for the development of antiviral therapeutics against COVID -19 (Krichel, Falke et al. 2020, Wu, Chen et al. 2020). Also, PLpro has been reported to have deubiquitinating (DUB) and deISGylating activities that inhibit the host innate immunity responses (Ratia, Kilianski et al. 2014, McClain and Vabret 2020). In this study, three potential allosteric sites on PLpro surface (**Figure S1**) were identified and targeted for mutagenesis to assess their role in the protease activity and thermal stability. Identification of important contacts in PLpro will aid in screening and developing antiviral drugs against COVID-19 and related coronaviruses diseases.

<u>Pocket 1</u>

The three predicted allosteric pockets are located at the opposite side of the PLpro active site. Pocket 1 is at the interface between the Ub1 and thumb domains. In pocket 1, D12 (Ub1 domain) and Y71 (thumb domain) are expected to form an inter-domain hydrogen bond between their side chains (**Figure 1A**). Interestingly, introduction of D12A decreased the relative enzyme activity and the catalytic turnover (k_{cat}) of PLpro as compared with WT. D12 is part of Ub1 domain that is important for the replication of SARS-CoV-2 as it has been shown to be involved in the processing of viral non-structural protein (nsp3) by the viral papain-like protease (PLpro). PLpro specifically cleaves the polyubiquitin chains of nsp3, which is necessary for viral replication. Therefore, Ub1 plays a critical role in the life cycle of SARS-CoV-2 and is a potential target for antiviral drug development.

On the other hand, Y71 is located in the thumb domain, which plays a critical role in substrate recognition, binding, and catalysis. Specifically, the thumb domain contains a groove that interacts with the substrate and helps to properly orient it for cleavage by the enzyme. Therefore, the thumb domain is essential for PLpro activity and is a potential target for antiviral drug development (Baez-Santos, St John et al. 2015, Osipiuk, Azizi et al. 2021). The alanine mutation in Y71 decreases the relative activity and catalytic turnover (*kcat*) of PLpro compared with WT. Similarly, Y83, from the thumb domain, interacts with Y56 from the Ub1 domain where Y83A mutant decreased PLpro activity by 90%, suggesting the importance of inter-domain interactions in maintaining PLpro activity. Surprisingly, the $t_{1/2}$ of Y71 increased by 2-fold when compared with WT while Y83 had a similar result to that of WT. This suggests that Y71A adopts a more robust conformational fold but has hijacked the activity of the protease.

<u>Pocket 2</u>

Pocket 2 is located at the interface of the thumb and palm domains of SARS-CoV-2 PLpro and includes a number of residues from the finger domain. In pocket 2, the mutants Q122A, Q133A, R140A, E238A, T277A and S278A, reduced PLpro activity by at least 50% with Q122A, T277A and S278A mutants having the lowest relative enzyme activity of 15.6 – 35% as compared to WT. The side chain of Q122 from the thumb domain forms an inter-domain hydrogen bond with the side chain of T277 from the palm domain. Also, the side chain of E238 (finger domain) forms an inter-domain interaction with the side chain of S309 (palm domain) as well as an intra-domain interaction with Q236 from the finger domain. On the other hand, Q133, R140 and S278 form intra-domain interactions with S278 whose alanine

mutant (S278A) reduced PLpro activity by 87% while Q133A and R140A reduced PLpro activity by 45% and 55%, respectively. In addition, K279A and S278A had a much lower $t_{1/2}$ than the WT. This indicates that K279A and S278A are of particular importance as it both destabilizes the enzyme and lowers the enzyme's activity. Interestingly, most mutations introduced in pocket 2 resulted in higher affinity to the substrate. However, a general decrease in catalytic efficiency is observed because of a decrease in K_{cat} amongst the pocket 2 mutants.

Pocket 3

Many residues found in pocket 3 had a drastic effect on the activity and stability of the enzyme. S212 and Y213 from the finger domain form a network of hydrogen bonds with Y305 and Y251 from the palm domain. Alanine mutations on S212, Y213 and Y305 either completely deactivates enzymatic activity or reduces it down to ~10%. S212A also has a half-life that is almost 3-fold less than that of WT and has reduced the catalytic efficiency of the enzyme by ~10-fold. This suggests that this cluster of hydrogen bond interactions is crucial for enzymatic function and stability.

On the other hand, K254 forms hydrogen bond interactions with E295, E252 and T257, all of which are from the palm domain. Expectedly, K254A drastically reduces the activity and the catalytic efficiency of the enzyme as it forms plenty of interactions with other intra-domain residues, suggesting that K254 is important in maintaining the proper fold of the palm domain. Conversely, E252 only forms an interaction with K254, so an alanine mutation on E252 had only reduced enzymatic activity and the catalytic efficiency down to ~60%.

Lastly, K306 forms an inter-domain hydrogen bond interaction with Q122 from the thumb domain. While this interaction is longer than the average distance of a hydrogen bond, a 50% decrease in enzymatic activity and catalytic efficiency is still observed.

In conclusion, enzyme titration experiments, kinetic studies, and determination of enzyme half-life suggests that there are several residues that are attractive for drug targeting as they either drastically reduce the protease's activity or stability (or both). Namely, these residues are D12 and Y83 in pocket 1; T277, S278, and K279 in pocket 2; and S212, Y213, Y305, and K254 in pocket 3. Since these pockets were identified by scanning the surface of the PLpro protein and they were identified to be located between protein domains, these findings support the notion that inter-domain interactions are more likely to contribute to enzyme stability and activity as compared with intra-domain interactions. The importance of the

allosteric residues in pocket 2 and pocket 3 has not been experimentally examined in previous studies, as only a few molecular docking and molecular dynamics studies have examined the binding modes of some potential inhibitors against PLpro. Q122, R140 and K279 have been expected to interact with anti-viral compounds, Indinavir and Lopinavir, through hydrogen-bonding interactions (Shiwani Rana 2021, Elfiky 2022). Another study on computational drug design predicted several residues of PLpro, K217, E252, T257, T259, S278, Y305 and K306 to be involved with bonded interactions with 3 potential drugs (Raj 2021).

References

Amin, S. A., K. Ghosh, S. Gayen and T. Jha (2021). "Chemical-informatics approach to COVID-19 drug discovery: Monte Carlo based QSAR, virtual screening and molecular docking study of some in-house molecules as papain-like protease (PLpro) inhibitors." J Biomol Struct Dyn **39**(13): 4764-4773.

Baez-Santos, Y. M., S. E. St John and A. D. Mesecar (2015). "The SARS-coronavirus papain-like protease: Structure, function and inhibition by designed antiviral compounds." Antiviral Research **115**: 21-38.

Barretto, N., D. Jukneliene, K. Ratia, Z. Chen, A. D. Mesecar and S. C. Baker (2005). "The papain-like protease of severe acute respiratory syndrome coronavirus has deubiquitinating activity." J Virol **79**(24): 15189-15198.

Bosken, Y. K., T. Cholko, Y. C. Lou, K. P. Wu and C. A. Chang (2020). "Insights Into Dynamics of Inhibitor and Ubiquitin-Like Protein Binding in SARS-CoV-2 Papain-Like Protease." Front Mol Biosci **7**: 174.

Calleja, D. J., G. Lessene and D. Komander (2022). "Inhibitors of SARS-CoV-2 PLpro." Front Chem **10**: 876212.

Cavasotto, C. N. and J. I. Di Filippo (2021). "In silico Drug Repurposing for COVID-19: Targeting SARS-CoV-2 Proteins through Docking and Consensus Ranking." Mol Inform **40**(1): e2000115.

Chadha, J., L. Khullar and N. Mittal (2022). "Facing the wrath of enigmatic mutations: a review on the emergence of severe acute respiratory syndrome coronavirus 2 variants amid coronavirus disease-19 pandemic." Environ Microbiol **24**(6): 2615-2629.

Chen, X., X. Yang, Y. Zheng, Y. Yang, Y. Xing and Z. Chen (2014). "SARS coronavirus papain-like protease inhibits the type I interferon signaling pathway through interaction with the STING-TRAF3-TBK1 complex." Protein Cell **5**(5): 369-381.

Elfiky, A. A. (2022). "SARS-CoV-2 Papain-like Protease as a Target for Anti-HCV and Anti-HIV Proteases: In silico Perspective." Systematic Reviews in Pharmacy **13**(4).

Ferreira, G. M., T. Pillaiyar, M. H. Hirata, A. Poso and T. Kronenberger (2022). "Inhibitor induced conformational changes in SARS-COV-2 papain-like protease." Sci Rep **12**(1): 11585.

Ferreira, J. C., S. Fadl, M. Ilter, H. Pekel, R. Rezgui, O. Sensoy and W. M. Rabeh (2021). "Dimethyl sulfoxide reduces the stability but enhances catalytic activity of the main SARS-CoV-2 protease 3CLpro." Faseb Journal **35**(8).

Gammeltoft, K. A., Y. Zhou, C. R. Duarte Hernandez, A. Galli, A. Offersgaard, R. Costa, L. V. Pham, U. Fahnøe, S. Feng, T. K. H. Scheel, S. Ramirez, J. Bukh and J. M. Gottwein (2021). "Hepatitis C Virus Protease Inhibitors Show Differential Efficacy and Interactions with Remdesivir for Treatment of SARS-CoV-2 In Vitro." Antimicrob Agents Chemother **65**(9): e0268020.

Gogoi, M., M. Borkotoky, S. Borchetia, P. Chowdhury, S. Mahanta and A. K. Barooah (2022). "Black tea bioactives as inhibitors of multiple targets of SARS-CoV-2 (3CLpro, PLpro and RdRp): a virtual screening and molecular dynamic simulation study." J Biomol Struct Dyn **40**(15): 7143-7166.

Jackson, C. B., M. Farzan, B. Chen and H. Choe (2022). "Mechanisms of SARS-CoV-2 entry into cells." Nat Rev Mol Cell Biol **23**(1): 3-20.

Jiang, H., P. Yang and J. Zhang (2022). "Potential Inhibitors Targeting Papain-Like Protease of SARS-CoV-2: Two Birds With One Stone." Front Chem **10**: 822785.
Jin, Z., X. Du, Y. Xu, Y. Deng, M. Liu, Y. Zhao, B. Zhang, X. Li, L. Zhang, C. Peng, Y. Duan, J. Yu, L. Wang, K. Yang, F. Liu, R. Jiang, X. Yang, T. You, X. Liu, X. Yang, F. Bai, H. Liu, X. Liu, L. W. Guddat, W. Xu, G. Xiao, C. Qin, Z. Shi, H. Jiang, Z. Rao and H. Yang (2020). "Structure of M(pro) from SARS-CoV-2 and discovery of its inhibitors." Nature **582**(7811): 289-293.
Kandeel, M., A. H. M. Abdelrahman, K. Oh-Hashi, A. Ibrahim, K. N. Venugopala, M. A. Morsy and M. A. A. Ibrahim (2021). "Repurposing of FDA-approved antivirals, antibiotics, anthelmintics, antioxidants, and cell protectives against SARS-CoV-2 papain-like protease." Journal of Biomolecular Structure and Dynamics **39**(14): 5129-5136.
Kaur, S. P. and V. Gupta (2020). "COVID-19 Vaccine: A comprehensive status report." Virus Res **288**: 198114.
Kim, D., J.-Y. Lee, J.-S. Yang, J. W. Kim, V. N. Kim and H. Chang (2020). "The Architecture of SARS-CoV-2 Transcriptome." Cell **181**(4): 914-921.e910.
Klemm, T., G. Ebert, D. J. Calleja, C. C. Allison, L. W. Richardson, J. P. Bernardini, B. G. Lu, N. W. Kuchel, C. Grohmann, Y. Shibata, Z. Y. Gan, J. P. Cooney, M. Doerflinger, A. E. Au, T. R. Blackmore, G. J. van der Heden van Noort, P. P. Geurink, H. Ovaa, J. Newman, A. Riboldi-Tunnicliffe, P. E. Czabotar, J. P. Mitchell, R. Feltham, B. C. Lechtenberg, K. N. Lowes, G. Dewson, M. Pellegrini, G. Lessene and D. Komander (2020). "Mechanism and inhibition of the papain-like protease, PLpro, of SARS-CoV-2." Embo j **39**(18): e106275.
Krichel, B., S. Falke, R. Hilgenfeld, L. Redecke and C. Uetrecht (2020). "Processing of the SARS-CoV pp1a/ab nsp7-10 region." Biochem J **477**(5): 1009-1019.
Lan, F. Y., R. Filler, S. Mathew, J. Buley, E. Iliaki, L. A. Bruno-Murtha, R. Osgood, C. A. Christophi, A. Fernandez-Montero and S. N. Kales (2020). "COVID-19 symptoms predictive of healthcare workers' SARS-CoV-2 PCR results." PLoS One **15**(6): e0235460.
Li, F. (2016). "Structure, Function, and Evolution of Coronavirus Spike Proteins." Annu Rev Virol **3**(1): 237-261.
Lim, C. T., K. W. Tan, M. Wu, R. Ulferts, L. A. Armstrong, E. Ozono, L. S. Drury, J. C. Milligan, T. U. Zeisner, J. Zeng, F. Weissmann, B. Canal, G. Bineva-Todd, M. Howell, N. O'Reilly, R. Beale, Y. Kulathu, K. Labib and J. F. X. Diffley (2021). "Identifying SARS-CoV-2 antiviral compounds by screening for small molecule inhibitors of Nsp3 papain-like protease." Biochemical Journal **478**(13): 2517-2531.
Lin, M. H., D. C. Moses, C. H. Hsieh, S. C. Cheng, Y. H. Chen, C. Y. Sun and C. Y. Chou (2018). "Disulfiram can inhibit MERS and SARS coronavirus papain-like proteases via different modes." Antiviral Res **150**: 155-163.
Luo, L., Q. Qiu, F. Huang, K. Liu, Y. Lan, X. Li, Y. Huang, L. Cui and H. Luo (2021). "Drug repurposing against coronavirus disease 2019 (COVID-19): A review." Journal of Pharmaceutical Analysis **11**(6): 683-690.
Lv, Z., K. E. Cano, L. Jia, M. Drag, T. T. Huang and S. K. Olsen (2021). "Targeting SARS-CoV-2 Proteases for COVID-19 Antiviral Development." Front Chem **9**: 819165.
Ma, C., Y. Hu, J. A. Townsend, P. I. Lagarias, M. T. Marty, A. Kolocouris and J. Wang (2020). "Ebselen, Disulfiram, Carmofur, PX-12, Tideglusib, and Shikonin Are Nonspecific Promiscuous SARS-CoV-2 Main Protease Inhibitors." ACS Pharmacol Transl Sci. **3**(6): 1265-1277.
Ma, C., M. D. Sacco, Z. Xia, G. Lambrinidis, J. A. Townsend, Y. Hu, X. Meng, T. Szeto, M. Ba, X. Zhang, M. Gongora, F. Zhang, M. T. Marty, Y. Xiang, A. Kolocouris, Y. Chen and J. Wang (2021). "Discovery of SARS-CoV-2 Papain-like Protease Inhibitors through a Combination of High-Throughput Screening and a FlipGFP-Based Reporter Assay." ACS Cent Sci **7**(7): 1245-1260.
McClain, C. B. and N. Vabret (2020). "SARS-CoV-2: the many pros of targeting PLpro." Signal Transduction and Targeted Therapy **5**(1): 223.
Mura, C., S. Preissner, R. Preissner and P. E. Bourne (2021). "A Birds-Eye (Re)View of Acid-Suppression Drugs, COVID-19, and the Highly Variable Literature." Front Pharmacol **12**: 700703.

Osipiuk, J., S. A. Azizi, S. Dvorkin, M. Endres, R. Jedrzejczak, K. A. Jones, S. Kang, R. S. Kathayat, Y. Kim, V. G. Lisnyak, S. L. Maki, V. Nicolaescu, C. A. Taylor, C. Tesar, Y. A. Zhang, Z. Zhou, G. Randall, K. Michalska, S. A. Snyder, B. C. Dickinson and A. Joachimiak (2021). "Structure of papain-like protease from SARS-CoV-2 and its complexes with non-covalent inhibitors." Nat Commun **12**(1): 743.
Pushpakom, S., F. Iorio, P. A. Eyers, K. J. Escott, S. Hopper, A. Wells, A. Doig, T. Guilliams, J. Latimer, C. McNamee, A. Norris, P. Sanseau, D. Cavalla and M. Pirmohamed (2019). "Drug repurposing: progress, challenges and recommendations." Nature Reviews Drug Discovery **18**(1): 41-58.
Quimque, M. T. J., K. I. R. Notarte, R. A. T. Fernandez, M. A. O. Mendoza, R. A. D. Liman, J. A. K. Lim, L. A. E. Pilapil, J. K. H. Ong, A. M. Pastrana, A. Khan, D. Q. Wei and A. P. G. Macabeo (2021). "Virtual screening-driven drug discovery of SARS-CoV2 enzyme inhibitors targeting viral attachment, replication, post-translational modification and host immunity evasion infection mechanisms." J Biomol Struct Dyn **39**(12): 4316-4333.
Raj, R. (2021). "Analysis of non-structural proteins, NSPs of SARS-CoV-2 as targets for computational drug designing." Biochem Biophys Rep **25**: 100847.
Ratia, K., A. Kilianski, Y. M. Baez-Santos, S. C. Baker and A. Mesecar (2014). "Structural Basis for the Ubiquitin-Linkage Specificity and deISGylating activity of SARS-CoV papain-like protease." PLoS Pathog **10**(5): e1004113.
Redhead, M. A., C. D. Owen, L. Brewitz, A. H. Collette, P. Lukacik, C. Strain-Damerell, S. W. Robinson, P. M. Collins, P. Schäfer, M. Swindells, C. J. Radoux, I. N. Hopkins, D. Fearon, A. Douangamath, F. von Delft, T. R. Malla, L. Vangeel, T. Vercruysse, J. Thibaut, P. Leyssen, T.-T. Nguyen, M. Hull, A. Tumber, D. J. Hallett, C. J. Schofield, D. I. Stuart, A. L. Hopkins and M. A. Walsh (2021). "Bispecific repurposed medicines targeting the viral and immunological arms of COVID-19." Scientific Reports **11**(1): 13208.
Rohaim, M. A., R. F. El Naggar, E. Clayton and M. Munir (2021). "Structural and functional insights into non-structural proteins of coronaviruses." Microb Pathog **150**: 104641.
Sargsyan, K., C.-C. Lin, T. Chen, C. Grauffel, Y.-P. Chen, W.-Z. Yang, H. S. Yuan and C. Lim (2020). "Multi-targeting of functional cysteines in multiple conserved SARS-CoV-2 domains by clinically safe Zn-ejectors." Chemical Science **11**(36): 9904-9909.
Shan, H., J. Liu, J. Shen, J. Dai, G. Xu, K. Lu, C. Han, Y. Wang, X. Xu, Y. Tong, H. Xiang, Z. Ai, G. Zhuang, J. Hu, Z. Zhang, Y. Li, L. Pan and L. Tan (2021). "Development of potent and selective inhibitors targeting the papain-like protease of SARS-CoV-2." Cell Chem Biol **28**(6): 855-865.e859.
Shetler, C. L., J. C. Ferreira, T. H. S. Cardoso, E. M. A. Silva, N. K. Saksena and W. M. Rabeh (2022). "Therapeutic potential of metal ions for COVID-19: insights from the papain-like protease of SARS-CoV-2." Biochem J **479**(20): 2175-2193.
Shiwani Rana, M. P. a. K. S. G. (2021). "Docking Studies with Multiple Molecular Targets Associated with SARSCoV-2 for Drug Repurposing." Coronaviruses **2**(8).
Smith, E., M. E. Davis-Gardner, R. D. Garcia-Ordonez, T. T. Nguyen, M. Hull, E. Chen, P. Baillargeon, L. Scampavia, T. Strutzenberg, P. R. Griffin, M. Farzan and T. P. Spicer (2020). "High-Throughput Screening for Drugs That Inhibit Papain-Like Protease in SARS-CoV-2." SLAS Discov **25**(10): 1152-1161.
V'Kovski, P., A. Kratzel, S. Steiner, H. Stalder and V. Thiel (2021). "Coronavirus biology and replication: implications for SARS-CoV-2." Nat Rev Microbiol **19**(3): 155-170.
Weglarz-Tomczak, E., J. M. Tomczak, M. Talma, M. Burda-Grabowska, M. Giurg and S. Brul (2021). "Identification of ebselen and its analogues as potent covalent inhibitors of papain-like protease from SARS-CoV-2." Sci Rep **11**(1): 3640.
WHO. (2022). "World Health Organization Coronavirus (COVID-19) Dashboard." Retrieved February 13, 2023, 2022, from https://covid19.who.int/.
Wu, D., T. Wu, Q. Liu and Z. Yang (2020). "The SARS-CoV-2 outbreak: What we know." Int J Infect Dis **94**: 44-48.
Wu, Y. C., C. S. Chen and Y. J. Chan (2020). "The outbreak of COVID-19: An overview." J Chin Med Assoc **83**(3): 217-220.

Xu, Y., K. Chen, J. Pan, Y. Lei, D. Zhang, L. Fang, J. Tang, X. Chen, Y. Ma, Y. Zheng, B. Zhang, Y. Zhou, J. Zhan and W. Xu (2021). "Repurposing clinically approved drugs for COVID-19 treatment targeting SARS-CoV-2 papain-like protease." International Journal of Biological Macromolecules **188**: 137-146.
Yang, X., X. Chen, G. Bian, J. Tu, Y. Xing, Y. Wang and Z. Chen (2014). "Proteolytic processing, deubiquitinase and interferon antagonist activities of Middle East respiratory syndrome coronavirus papain-like protease." J Gen Virol. **95**(3): 614-626.
Zhang, Q., R. Xiang, S. Huo, Y. Zhou, S. Jiang, Q. Wang and F. Yu (2021). "Molecular mechanism of interaction between SARS-CoV-2 and host cells and interventional therapy." Signal Transduct Target Ther **6**(1): 233.
Zhao, Y., X. Du, Y. Duan, X. Pan, Y. Sun, T. You, L. Han, Z. Jin, W. Shang, J. Yu, H. Guo, Q. Liu, Y. Wu, C. Peng, J. Wang, C. Zhu, X. Yang, K. Yang, Y. Lei, L. W. Guddat, W. Xu, G. Xiao, L. Sun, L. Zhang, Z. Rao and H. Yang (2021). "High-throughput screening identifies established drugs as SARS-CoV-2 PLpro inhibitors." Protein & Cell **12**(11): 877-888.

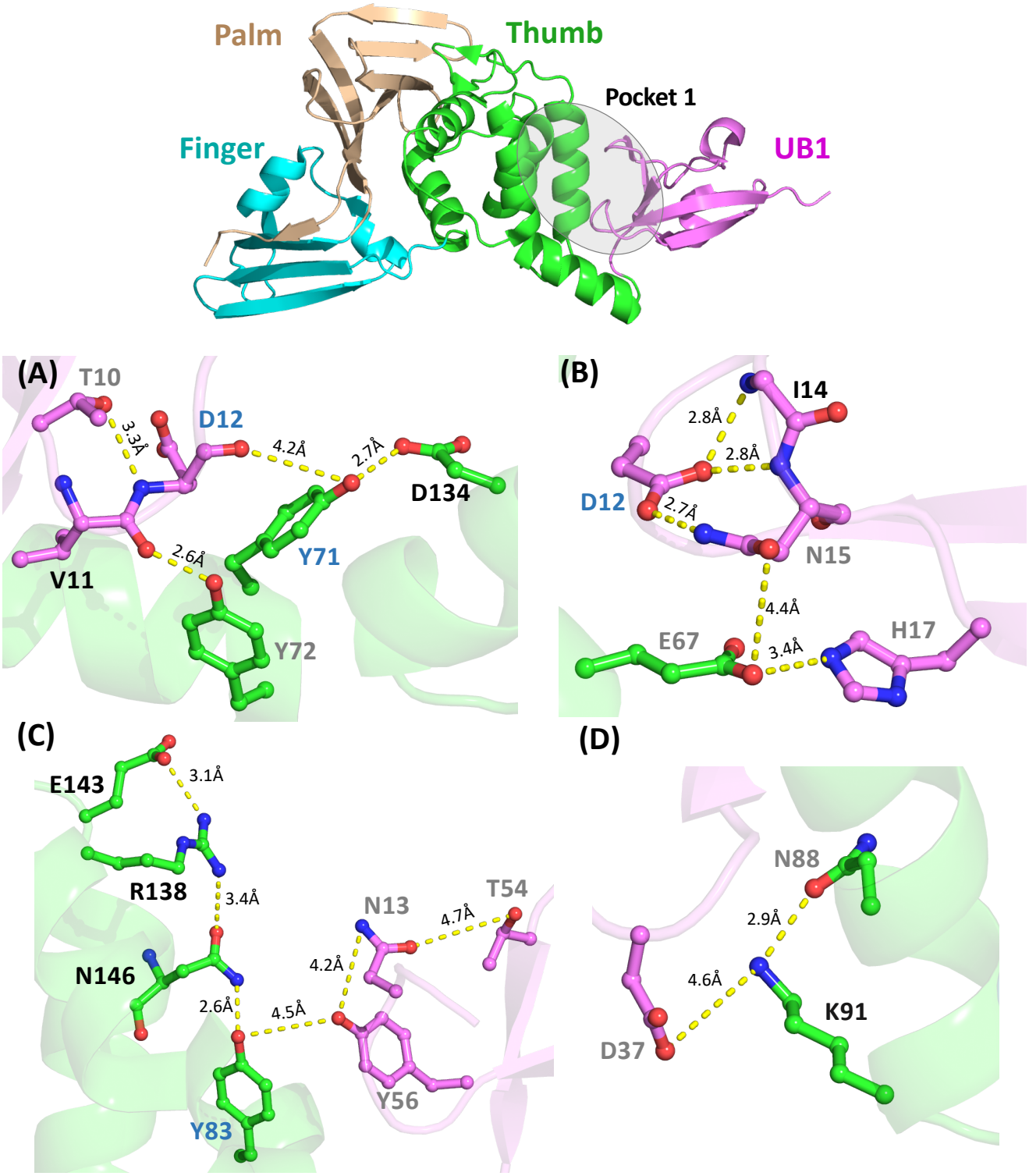

Figure 1: Key residues at the computationally predicted allosteric site, pocket 1, of SARS-CoV-2 Plpro. A cartoon representation of the structural fold of the PLpro monomer is shown at the top and colored by domains: Ub1 (1 – 60) in violet, thumb domain (61 – 176) in green, finger domain (177 – 238) in cyan, and the palm domain (239 – 315) in light orange. The amino acid residues presented here belong to pocket 1 that is located at in the interface between Ub1 and thumb domains of SARS-CoV-2 PLpro. Panels (**A – D**) present the detailed interactions of pocket 1 residues that form intra- and inter-domain polar side chain interactions with other residues. Overall, all allosteric amino acids residues mentioned here have been mutated to alanine to determine their role in the catalytic function of PLpro of SARS-CoV-2. Amino acid residues that inactivated PLpro are labelled in red, partially reduced its proteolytic activity (<60%) in blue, and those that did not affect the activity in black. The figure was generated using PDB entry 6WZU in PyMol (Schrodinger LLC).

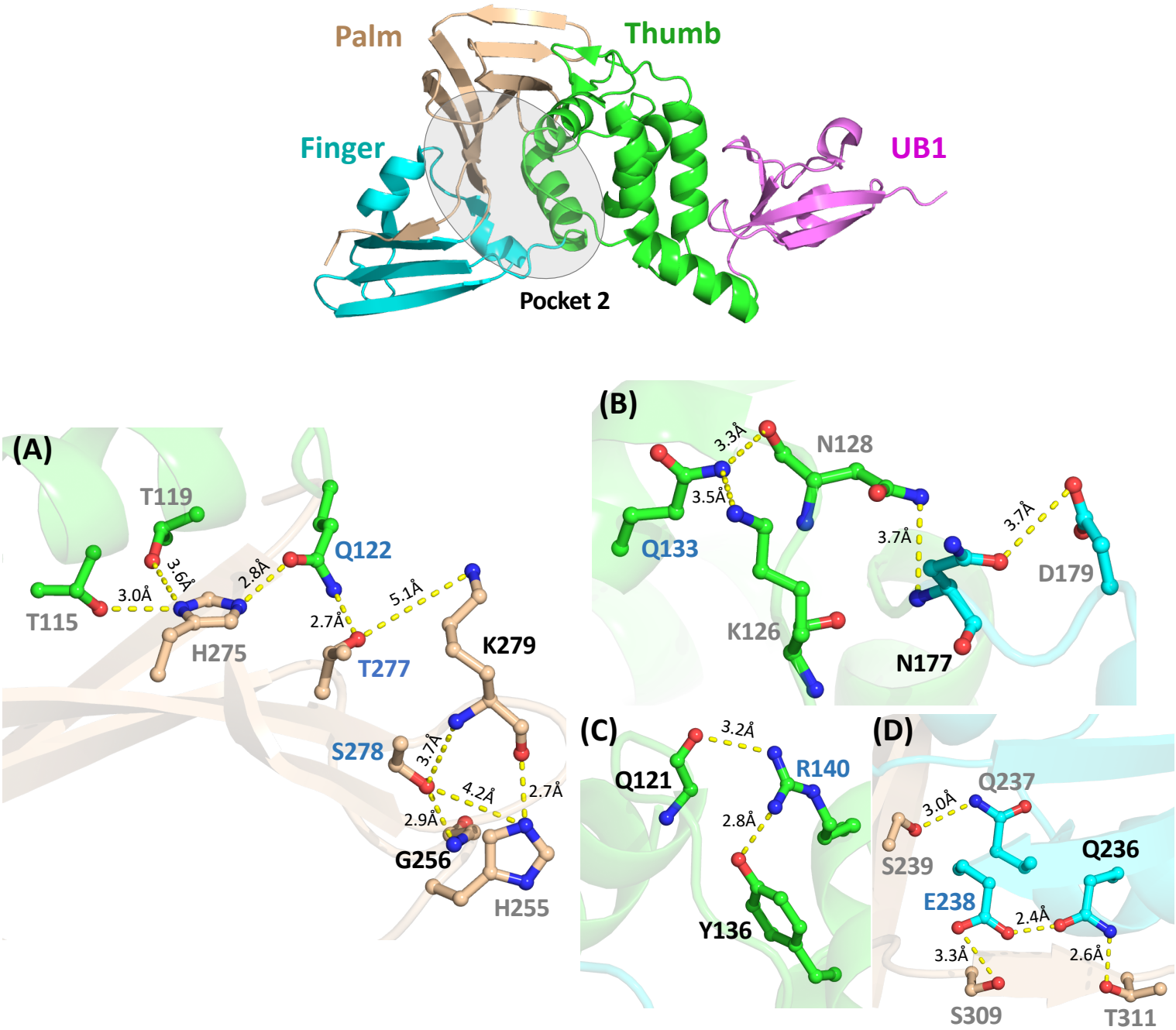

Figure 2: Key residues at the computationally predicted allosteric site, pocket 2, of SARS-CoV-2 Plpro. A cartoon representation of the structural fold of the PLpro monomer is shown at the top. The color code is identical to that in Figure 1. The amino acid residues presented here belong to pocket 2 that is located between the thumb and palm domains and only a few residues from the finger domain of SARS-CoV-2 PLpro. Panels (**A – D**) present the detailed interactions of pocket 2 residues that form intra- and inter-domain polar side chain interactions with other residues. Overall, all allosteric amino acids residues mentioned here have been mutated to alanine to determine their role in the catalytic function of PLpro of SARS-CoV-2. Amino acid residues that inactivated PLpro are labelled in red, partially reduced its proteolytic activity (<60%) in blue, and those that did not affect the activity in black. The figure was generated using PDB entry 6WZU in PyMol (Schrodinger LLC).

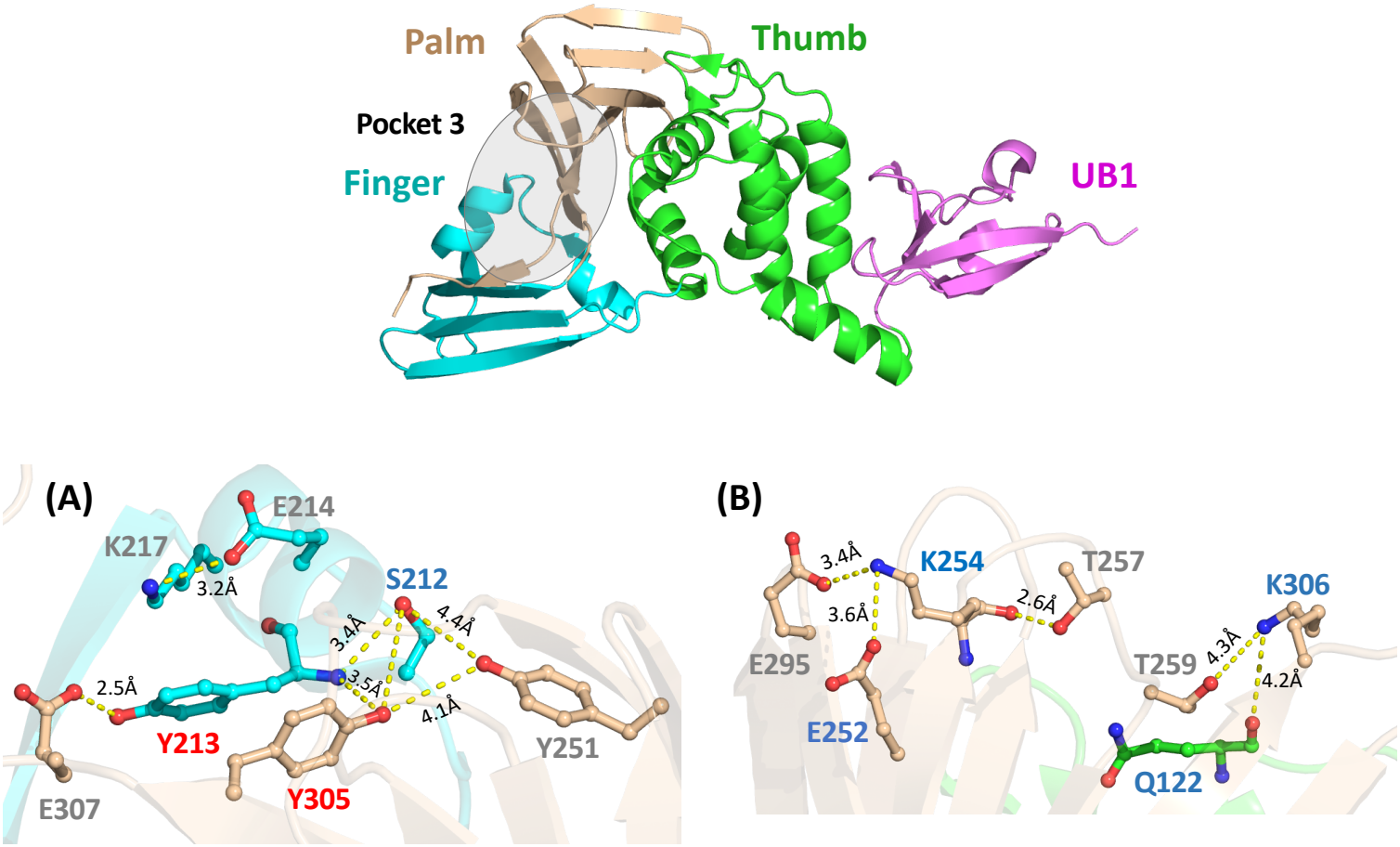

Figure 3: Key residues at the computationally predicted allosteric site, pocket 3, of SARS-CoV-2 Plpro. A cartoon representation of the structural fold of the PLpro monomer is shown at the top. The color code is identical to that in Figure 1. The amino acid residues presented here belong to pocket 3 that is located at the interface between the finger and palm domains of SARS-CoV-2 PLpro. Panels **(A)** and **(B)** present the detailed interactions of pocket 3 residues that form intra- and inter-domain polar side chain interactions with other residues. Overall, all allosteric amino acids residues mentioned here have been mutated to alanine to determine their role in the catalytic function of PLpro of SARS-CoV-2. Amino acid residues that inactivated PLpro are labelled in red, partially reduced its proteolytic activity (<60%) in blue, and those that did not affect the activity in black. The figure was generated using PDB entry 6WZU in PyMol (Schrodinger LLC).

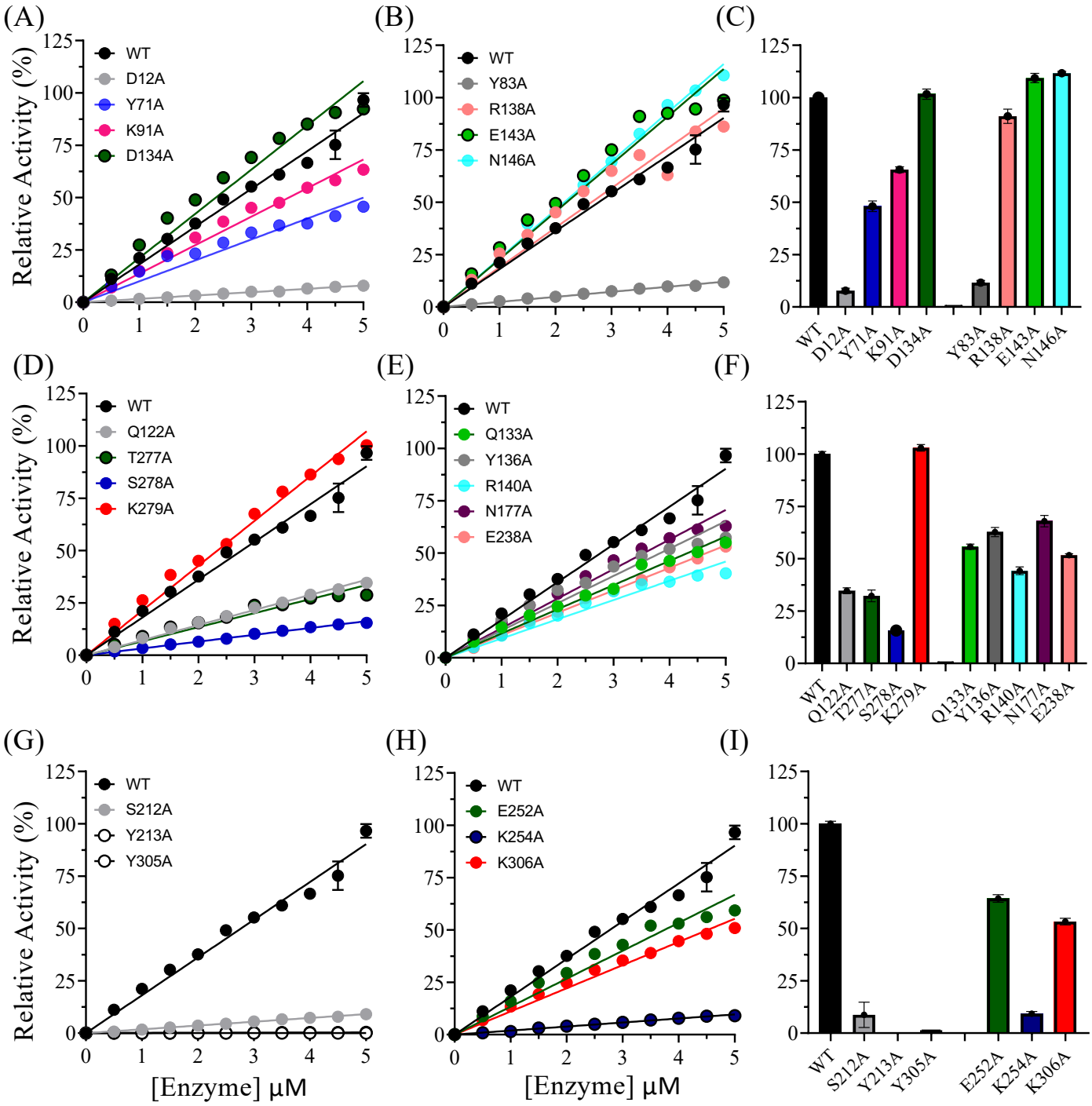

Figure 4: The effect of alanine substitutions at the three pockets on the relative activity of PLpro. Relative enzyme activity was measured at increasing enzyme concentrations (0.0–5 μM) and a fixed peptide substrate concentration of 200 μM in assay, at 25° C, in a buffer containing 20 mM HEPES, pH 7.5, 100 mM NaCl, 1 mM EDTA, 1 mM TCEP. The relative enzyme activities of mutants with alanine substitutions at residues in the pockets of PLpro were obtained by normalizing the cleavage rates of each mutant to that of the WT enzyme. The enzymatically active mutants are represented by filled colored circles, whereas inactive mutants are represented by open black circles. WT activity is shown by black filled circles. (**A** – **B**) Pocket 1. **(D-E)** Pocket 2 and **(G-H)** Pocket 3**.** Bar plot of the relative enzyme activities of the enzymatically active mutants compared to the WT enzyme. (**C**) Pocket 1. **(F)** Pocket 2 and **(I)** Pocket 3. The data are presented as the mean ± SD, n = 3.

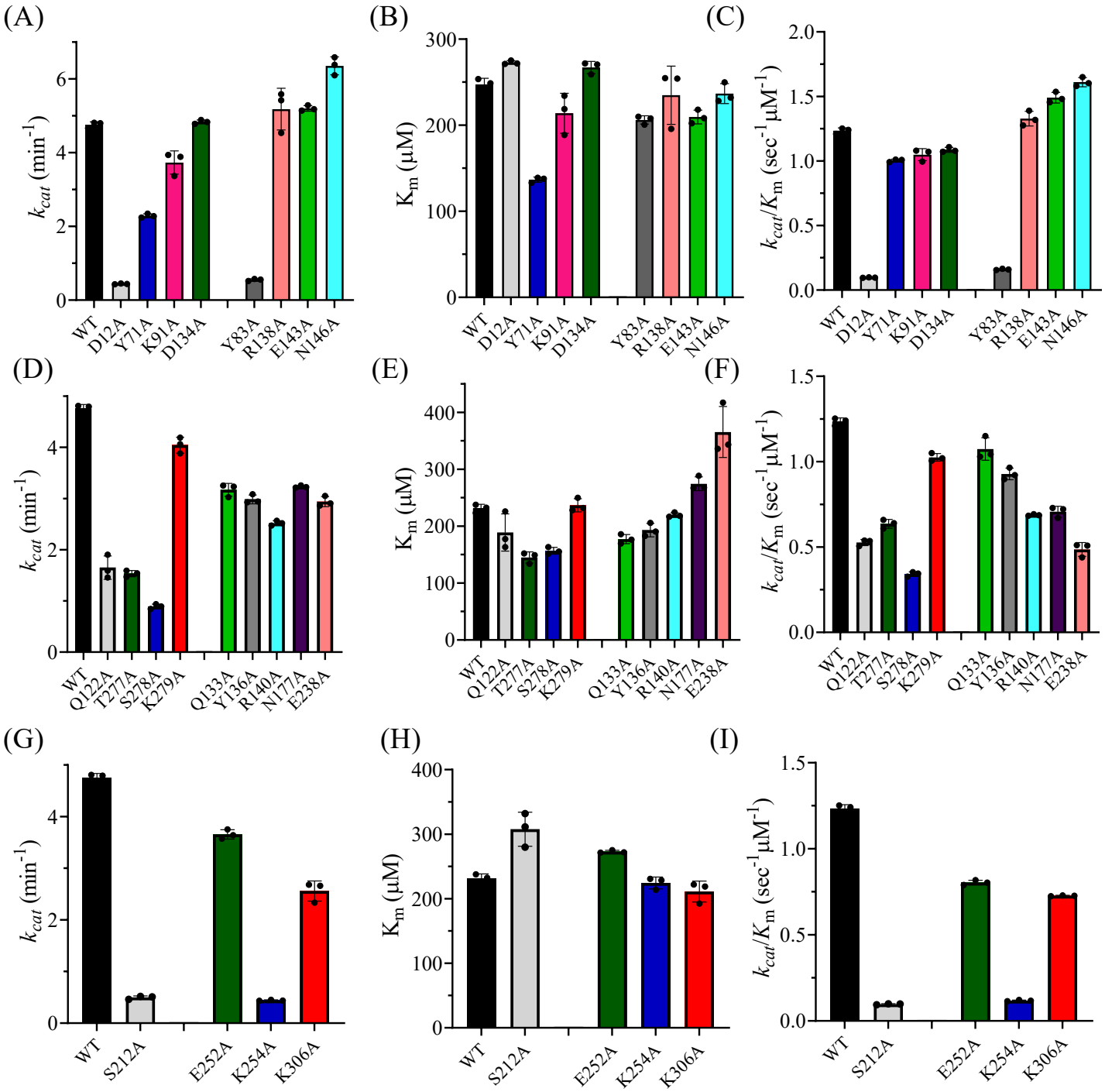

Figure 5: Kinetic characterization of the enzymatically active PLpro mutants. Bar plots of the kinetic parameters k_{cat}, K_m, and k_{cat}/K_m for WT PLpro (black bars), active site mutants (colored bars). The initial velocity rates were measured at 25 °C and in the in buffer containing 20 mM HEPES, pH 7.5, 100 mM NaCl, 1 mM EDTA, 1 mM TCEP. (**A** – **C**) Pocket 1. **(D-F)** Pocket 2 and **(G-I)** Pocket 3. The data points represent the mean ± SD of triplicate measurements.

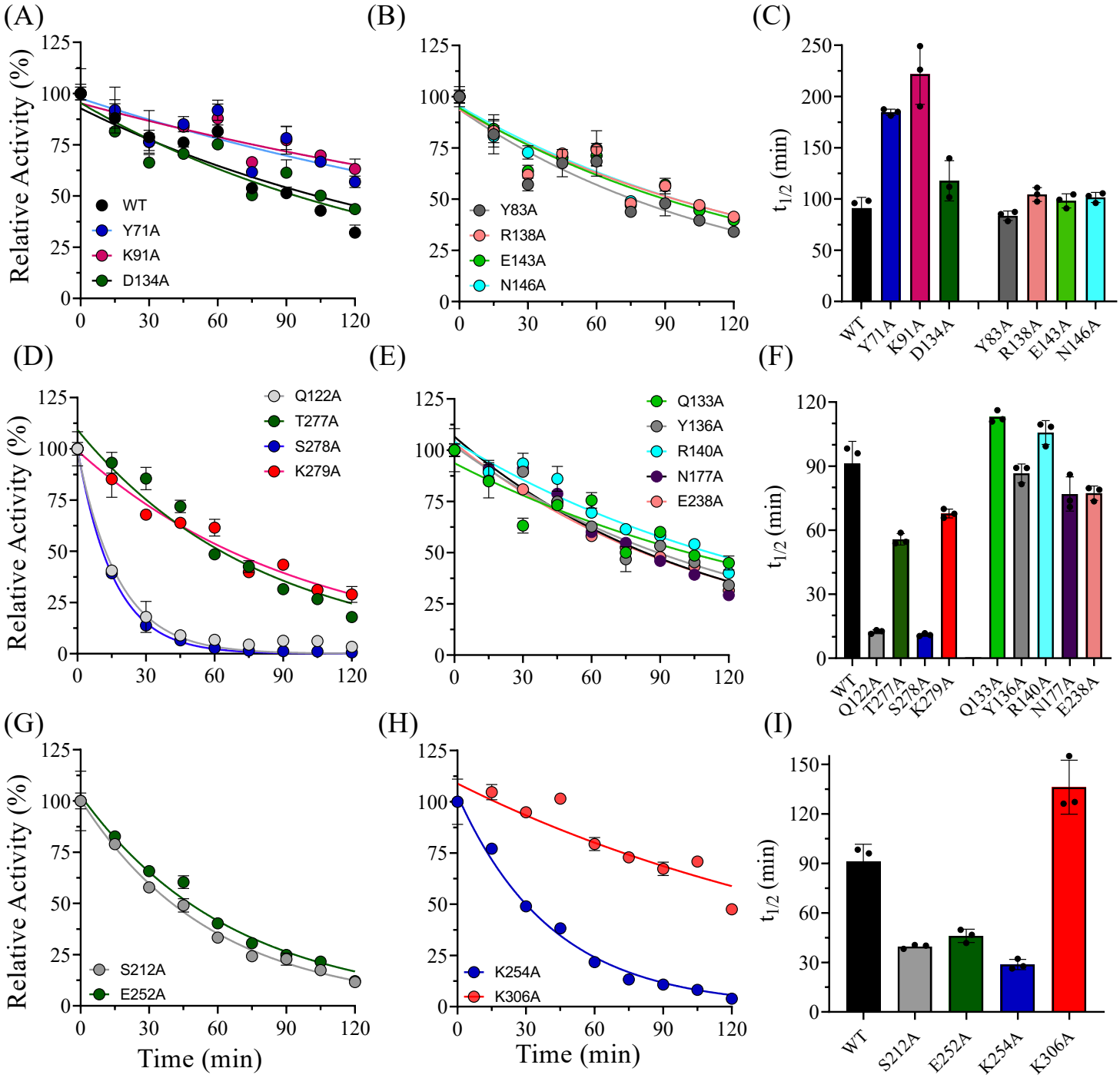

Figure 6. Calculation of Half-life ($t_{1/2}$) In 15 minute time intervals, the remaining enzymatic activity of each PLpro variant was measured while incubating the enzyme at 37 °C for two hours. **(A-C)** Pocket 1. **(D-F)** Pocket 2. **(G-I)** Pocket 3. Data are presented as mean ± S.D., n=3.